Journal of Luminescence 220 (2020) 116995

Contents lists available at ScienceDirect

Journal of Luminescence

journal homepage: http://www.elsevier.com/locate/jlumin

Enhanced green emission and thermal stability of $Ba_3Si_6O_{12}N_2:Eu^{2+}$ by Ce^{3+}/P^{5+}-doping: Unity energy transfer, charge compensation and lattice strain release

Jiarui Hao [a], Mengxuan Tao [a], Zhiyu Gao [a], Shuoting Chen [a], Yixin Liu [a], Hongquan Wang [a], Yi Wei [a], Maxim S. Molokeev [b,c,d], Guogang Li [a,*]

[a] Engineering Research Center of Nano-Geomaterials of Ministry of Education, Faculty of Materials Science and Chemistry, China University of Geosciences, 388 Lumo Road, Wuhan, 430074, PR China
[b] Laboratory of Crystal Physics, Kirensky Institute of Physics, SB RAS, Krasnoyarsk, 660036, Russia
[c] Department of Physics, Far Eastern State Transport University, Khabarovsk, 680021, Russia
[d] Siberian Federal University, Krasnoyarsk, 660041, Russia

ARTICLE INFO

Keywords:
Oxonitridosilicate
Green phosphor
Unity energy transfer
Charge compensation
Thermal stability improvement

ABSTRACT

To optimize luminescence properties of oxonitridosilicate phosphors are extremely necessary for improving lighting quality of white light-emitting diodes (WLEDs). Herein, we designed Ce^{3+}, Eu^{2+} codoping and $P^{5+}\leftrightarrow Si^{4+}$ substitution in the presentative $Ba_3Si_6O_{12}N_2:Eu^{2+}$ green phosphor to realize an enhancement of luminescence efficiency and thermal stability. Rietveld refinement results of Ce^{3+}, Eu^{2+}, P^{5+}-doped $Ba_3Si_6O_{12}N_2$ (BSON) confirmed the formation of pure trigonal phase (*P*-3) of $Ba_3Si_6O_{12}N_2$ and the successful doping of Ce^{3+}, Eu^{2+}, P^{5+} ions. Ce^{3+} and Eu^{2+} ions randomly occupy two Ba crystallographic sites. Interestingly, a near unity energy transfer (ET, ~100%) from Ce^{3+} ions to Eu^{2+} ions is observed. Meanwhile, the doping of P^{5+} ions into BSON also helps improving the luminescence efficiency and thermal stability, which should be attributed to the charge compensation and the relax of lattice strain. In addition, the white light emitting diodes (WLEDs) fabricated by employing P^{5+}-doped BSON: Eu^{2+} present a better electroluminescence performance than BSON: Eu^{2+}. This study could serve as a guide in developing optimized oxonitridosilicates phosphors with improved luminescence performances based on complete energy transfer and lattice variations in local coordination environments through cation substitutions, and the as-prepared Ce^{3+}/P^{5+}-codoped $Ba_3Si_6O_{12}N_2:Eu^{2+}$ could be an excellent green-emitting phosphor for UV-to-Visible LED chips pumped WLEDs.

1. Introduction

Phosphor-converted white light-emitting diodes (pc-WLEDs) as one of the most famous solid-state lighting sources has extensively penetrated into our daily lives due to the high luminescence efficiency, low energy consumption, durability and eco-friendly features [1]. Typical pc-WLEDs composed of 460 nm blue InGaN chips with yellow $Y_3Al_5O_{12}:Ce^{3+}$ phosphor easily encounter high correlated color temperatures (CCT > 4500 K) and poor color-rendering indices (Ra < 75) due to the absence of red components in spectral profile [2]. A feasible method to realize high-quality warm white lighting is to combine near ultraviolet light (n-UV, 380–420 nm) LED chips with trichromatic emitting phosphors [3–9]. How to further improve the luminous efficiency of trichromatic phosphor materials is the key and difficult point to achieve high quality white LED lighting, and has being always the research hotspot in the field of luminescent materials [10–12]. Among various inorganic phosphor materials, green emitting phosphors commonly demonstrate the main contribution to the luminescence efficiency of WLEDs compared with another employed luminescence materials such as blue and red phosphor materials [13–15]. Therefore, the development of highly efficient green phosphor materials is extremely necessary [16–19].

So far, many rare earth activated oxonitridosilicate compounds such as $Ba_2Si(O,N)_4:Eu^{2+}$ [20], $Ba_3Si_6O_{12}N_2:Eu^{2+}$ [21], $SrSi_2O_2N_2:Eu^{2+}$ [22], β-SiAlON:Eu^{2+} [23], $Sr_{1-x}Ca_xYSi_4N_7:Eu^{2+}$ [24], $La_3Si_6N_{11}:Ce^{3+}$[25] and so on have been intensively explored as advanced yellow emitting

* Corresponding author.
E-mail address: ggli@cug.edu.cn (G. Li).

https://doi.org/10.1016/j.jlumin.2019.116995
Received 17 August 2019; Received in revised form 8 December 2019; Accepted 23 December 2019
Available online 24 December 2019

materials under blue and/or UV light excitation. The presence of coordinated nitrogen in host framework means an increase the covalence of host lattices, which not only improves the thermal stability but also could realize an emission adjustment [26,27]. Although excellent luminescence properties such as high luminescence efficiency, superior thermal stability and long-wavelength emission are usually expected in rare earth activated oxonitridosilicates, not all superior performances are concentrated on one phosphor. Many current oxonitridosilicate phosphors suffer different drawbacks, for example, inappropriate emission position and full width at half maxima (fwhm), low efficiency and poor thermal stability [28]. To promote the practical application in WLEDs of abovementioned oxonitridosilicate phosphors, it is necessary to optimize and improve the luminescence efficiency and thermal stability as well as to tune the spectral properties [29–31].

Because the 5d–4f transition emission of Eu^{2+} is closely related to the coordination environment of host; hence, the modifications of crystal field strength, symmetry, covalency, and polarizability of activator–ligand bonds in Eu^{2+}-activated phosphors have been widely concerned to optimize phosphor materials for the lighting requirements [32–38]. In various luminescence regulation strategies, cation substitutions have been widely considered to modify host lattice for achieving highly efficient luminescence materials [38–45]. In this work, we synthesized a series of Ce^{3+}/P^{5+}-codoped $Ba_3Si_6O_{12}N_2$:Eu^{2+} green phosphor by a high-temperature solid state reaction. The structural evolution and crystallographic site occupancy were analyzed by Rietveld refinement. By designing Ce^{3+}→Eu^{2+} energy transfer and P^{5+}↔Si^{4+} cation substitution, an obvious enhancement of luminescence efficiency and thermal stability of the studied phosphors were observed. Interestingly, a near unity energy transfer (ET, ~100%) from Ce^{3+} ions to Eu^{2+} ions was observed in the BSON: Ce^{3+}, Eu^{2+} system, and the ET mechanism was investigated. Except for ET, the doping of P^{5+} ions into BSON also help improve the luminescence efficiency and thermal stability, and the corresponding improvement mechanism was discussed. Finally, the as-prepared P^{5+}-doped BSON: Eu^{2+} phosphors were fabricated to WLEDs for assessing the electroluminescence performance. This study targets to optimize the luminescence efficiency and thermal stability of current rare earth activated oxonitridosilicate phosphors through designing complete energy transfer and modify lattice environment based on cation substitutions.

2. Experimental section

2.1. Materials and synthesis

The Ce^{3+}, Eu^{2+} and P^{5+}-doped $Ba_3Si_6O_{12}N_2$ oxonitridosilicate compounds were prepared *via* a traditional high-temperature solid state reaction. The raw materials were $BaCO_3$ (J.T. Baker Corporation, 99.95%), SiO_2 (Sigma-Aldrich, 99.999%), Si_3N_4 (Sigma-Aldrich, 99.99%), Eu_2O_3 (Sigma-Aldrich, 99.99%), CeO_2 (Aladdin, 99.99%), and $NH_4H_2PO_4$ (Aladdin, 99.9%). Stoichiometric amounts of raw materials were weighed according to the designed doping ratio, and then were mixed and ground together for 30 min with appropriate amount of absolute ethanol in an agate mortar with agate pestle. The forming mixtures were transferred into aluminium oxide crucibles. After an annealing treatment in a horizontal tube furnace at 1400 °C for 8 h under a reduced atmosphere of H_2 (10%)−N_2 (90%), the obtained samples were again ground, yielding the resulting phosphor powders.

2.2. LED fabrication

WLEDs devices were fabricated by combining the representative green BSON: $Eu^{2+}_{0.15}$, $P^{5+}_{0.09}$ and BSON: $Eu^{2+}_{0.15}$ phosphors, blue BAM and red $CaAlSiN_3$:Eu^{2+} phosphors with 370 nm InGaN chips. The proper amounts of phosphors were added into the epoxy resins (A:B = 1:1) and mixed thoroughly for 20 min. The acquired mixture was smoothly coated on the surface of InGaN chips and dried at 70 °C to produce resulting WLEDs. All measurements were carried out at 20 mA drive current.

2.3. Characterization

The crystal structure and phase purity of the as-prepared samples were characterized and analyzed by X-ray powder (XRD) patters, which were performed on a D8 Focus diffractometer at as canning rate of 1° min^{-1} in the 2θ range from 10° to 120° with Ni-filtered Cu-Kα (λ = 1.540598 Å) at 40 kV tube voltage and 40 mA tube current. XRD Rietveld profile refinements of the structural models and texture analysis were performed with the use of General Structure Analysis System (GSAS) software. The morphologies, energy-dispersive X-ray spectrum (EDS) and elemental mapping analysis of the samples were inspected using a field emission scanning electron microscope (FE-SEM, S-4800, Hitachi). The photoluminescence excitation (PLE) and emission (PL) spectra were measured by Edinburg fluorescence spectrophotometer (FLSP-920) equipped with a 450 W xenon lamp as the excitation source. The luminescence thermal stability was measured by FLSP-920 spectrometer using a combined setup consisting of a Xe-lamp, a Hamamatsu MPCD-7000 multichannel photodetector and a computer-controlled heater. X-ray absorption near edge structure (XANES) of Eu L3-edge was recorded with a wiggler beamline BL17C at National Synchrotron Radiation Research Center in Hsinchu, Taiwan. The photoluminescence quantum yield (QY) was measured by absolute PL quantum yield measurement system C9920-02 (Hamamatsu photonics K·K., Japan). The photoluminescence decay curves were obtained from a Lecroy Wave Runner 6100 Digital Osilloscope (1 GHz) using a tunable laser (pulse width = 4 ns, gate = 50 ns) as the excitation (Contimuum Sunlite OPO). The electroluminescence (EL) performances of the w-LEDs were measured by Starspec SSP6612.

3. Results and discussion

According to some previous reports, $Ba_3Si_6O_{12}N_2$ matrix possesses a trigonal structure that is composed of 8-membered Si–(O,N) and 12-membered Si–O rings [46]. The corner sharing SiO_3N tetrahedra forming corrugated layers between which the Ba^{2+} ions are located. Each N atom connects three Si atoms, and each O atom connects two Si atoms [47]. The phase purity and crystal structure of the as-prepared Ce^{3+}, Eu^{2+}, P^{5+}-doped $Ba_3Si_6O_{12}N_2$ samples are analyzed using X-ray diffraction (XRD). Fig. 1a shows the typical XRD patterns of BSON: $Ce^{3+}_{0.05}$, BSON: $Eu^{2+}_{0.15}$, BSON: $Ce^{3+}_{0.05}$, $Eu^{2+}_{0.15}$, BSON: $Eu^{2+}_{0.15}$, $P^{5+}_{0.09}$ and BSON: $Eu^{2+}_{0.15}$, $P^{5+}_{0.15}$ samples. As expectedly, the XRD peaks of above samples all can be ascribed to a trigonal phase (*P*-3) of $Ba_3Si_6O_{12}N_2$ (ICSD No. 985697) and no diffraction peaks of any other phases are detected [21]. The results indicate that the successful synthesis of the target compounds and the successful doping of Ce^{3+}, Eu^{2+} and P^{5+} ions. In view of a loose lattice environment and similar ion radius compared with Ba^{2+} sites (r = 1.42 Å, coordination number (CN) = 8), Ce^{3+} (r = 1.143 Å, CN = 8) and Eu^{2+} (r = 1.25 Å, CN = 8) ions more easily occupy Ba^{2+} crystallographic sites. While P^{5+} ions (r = 0.17 Å, CN = 4) enter into Si^{4+} sites (r = 0.26 Å, CN = 4) in $Ba_3Si_6O_{12}N_2$ host. The introduction of Ce^{3+}, Eu^{2+} and P^{5+} ions maintains the phase purity of $Ba_3Si_6O_{12}N_2$, and does not change its crystal structure. The enlarged XRD patterns around 2θ = 27.5° (Figs. 1b) and 2θ = 30.9° (Fig. 1c) of presentative BSON: $Eu^{2+}_{0.15}$, $P^{5+}_{0.09}$ and BSON: $Eu^{2+}_{0.15}$, $P^{5+}_{0.15}$ samples exhibit a big angel shift with the increase of P-substituted content. Since the smaller ion radius of P^{5+} ions than Si^{4+} ions, this result confirms that P^{5+} ions successfully replace at the Si^{4+} sites in $Ba_3Si_6O_{12}N_2$ matrix.

In order to further investigate the crystal structure of Ce^{3+}, Eu^{2+}, P^{5+}-doped BSON samples, Rietveld refinement of the representative $Ba_{2.85}Eu_{0.15}Si_6O_{12}N_2$ is performed by using TOPAS 4.2 [48]. Fig. 1d reveals that all peaks are indexed by trigonal cell (*P*-3) with parameters close to $Ba_3Si_6O_{12}N_2$ [49]. This crystal structure was taken as starting

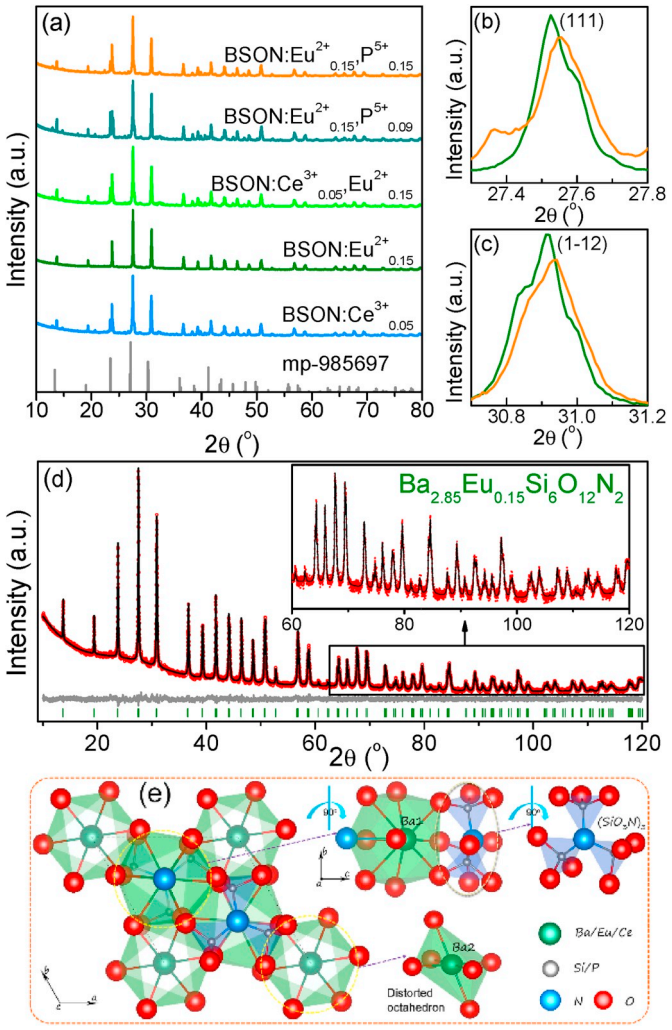

Fig. 1. (a) The typical XRD patterns of BSON: $Ce^{3+}_{0.05}$, BSON: $Eu^{2+}_{0.15}$, BSON: $Ce^{3+}_{0.05}$, $Eu^{2+}_{0.15}$, BSON: $Eu^{2+}_{0.15}$, $P^{5+}_{0.09}$ and BSON: $Eu^{2+}_{0.15}$, $P^{5+}_{0.15}$ samples. The standard XRD card of $Ba_3Si_6O_{12}N_2$ (mp-985697) is shown as reference. Enlarged XRD patterns of BSON: $Eu^{2+}_{0.15}$ and BSON: $Eu^{2+}_{0.15}$, $P^{5+}_{0.09}$ samples around (b) 2θ = 27.5° and (c) 2θ = 31°, which corresponds to the (111) and (1–12) crystal planes, respectively. (d) Rietveld fit of the XRD pattern of the presentative BSON: $Eu^{2+}_{0.15}$ sample using TOPAS 4.2. Experimental (black solid line), calculated (red dot line) XRD patterns and their difference (gray solid line) for BSON: $Eu^{2+}_{0.15}$. The green short vertical lines show the positions of Bragg reflections of the calculated pattern. (e) Schematic diagram of the crystal structure of Ce^{3+}, Eu^{2+}, P^{5+}-doped $Ba_3Si_6O_{12}N_2$.

model for Rietveld refinement. There are two Ba sites that one is coordinated with six oxygen atoms to form distortedoctahedron and the other is capped with nine oxygen atoms and a nitrogen atom in the asymmetric part of the unit cell and both these sites were occupied by Ba and Eu ions with fixed occupations according to suggested formula (Fig. 1e) [50]. Refinement is stable and give low *R*-factors (Table 1), indicating the formation of pure $Ba_3Si_6O_{12}N_2$ phase. Coordinates of atoms and main bond lengths are collected in Tables 2 and 3, respectively. The cell volume of doped compound V = 315.538 (7) Å^3 is smaller than the cell volume of the host $Ba_3Si_6O_{12}N_2$, V = 316.94 Å^3. This fact is in a good agreement with the smaller ion radii of Eu^{2+} ions in comparison with Ba^{2+} ions. These results mean that the co-doping ions do not cause any significant change in the host structure, which clearly suggests that the activator and co-activator have been incorporated in the lattice.

Fig. 2 shows the SEM images, element mapping images and EDS of the representative BSON: $Ce^{3+}_{0.05}$, $Eu^{2+}_{0.15}$ and BSON: $Eu^{2+}_{0.15}$, $P^{5+}_{0.09}$

Table 1
Main parameters of processing and refinement of the $Ba_{2.85}Eu_{0.15}Si_6O_{12}N_2$ (BSON: $Eu^{2+}_{0.15}$) sample.

Compound	$Ba_{2.85}Eu_{0.15}Si_6O_{12}N_2$ (BSON: $Eu^{2+}_{0.15}$)
Space group	*P*-3
a, Å	7.50382 (7)
c, Å	6.47076 (7)
V, Å^3	315.538 (7)
Z	1
2*θ*-interval, °	10–120
R_{wp}, %	4.32
R_p, %	3.30
R_{exp}, %	3.42
χ [2]	1.27
R_B, %	1.18

Table 2
Fractional atomic coordinates and isotropic displacement parameters (Å^2) of $Ba_{2.85}Eu_{0.15}Si_6O_{12}N_2$ (BSON: $Eu^{2+}_{0.15}$).

	x	*y*	*z*	B_{iso}	Occ.
Ba1	0	0	0	0.77 (6)	0.95
Eu1	0	0	0	0.77 (6)	0.05
Ba2	1/3	2/3	0.1035 (2)	0.49 (4)	0.95
Eu2	1/3	2/3	0.1035 (2)	0.49 (4)	0.05
Si1	0.4046 (4)	0.2378 (4)	0.3872 (6)	0.50 (7)	1
N1	1/3	2/3	0.567 (2)	0.50 (10)	1
O1	0.6867 (13)	0.0027 (9)	0.601 (1)	0.50 (10)	1
O2	0.6412 (12)	0.7050 (13)	0.833 (1)	0.50 (10)	1

Table 3
Main bond lengths (Å) of $Ba_{2.85}Eu_{0.15}Si_6O_{12}N_2$ (BSON: $Eu^{2+}_{0.15}$).

Ba1–O2^{i}	2.713 (8)	Si1–N1^{ii}	1.749 (3)
Ba2–O1^{ii}	3.197 (7)	Si1–O1^{iv}	1.580 (6)
Ba2–O2^{iii}	2.797 (7)	Si1–O1^{v}	1.745 (8)
Ba2–O2^{ii}	2.918 (8)	Si1–O2^{ii}	1.574 (7)

Symmetry codes: (i) *x*-1, *y*-1, *z*-1; (ii) -*x*+1, -*y*+1, -*z*+1; (iii) *x*, *y*, *z*-1; (iv) -*x*+1, -*y*, -*z*+1; (v) -*x* + *y*+1, -*x*+1, *z*.

samples. Clearly, the studied samples are irregular bulk particle with a size about 20–30 μm. Fig. 2a and b also gives the SEM element mapping images of BSON: $Ce^{3+}_{0.05}$, $Eu^{2+}_{0.15}$ and BSON: $Eu^{2+}_{0.15}$, $P^{5+}_{0.09}$ samples, respectively, which demonstrates that the sample contains Ba–Si–*O*–N–Ce-Eu and Ba–Si–*O*–N–P-Eu elements, and they evenly distribute in the whole sample. Furthermore, the SEM-EDS analysis of BSON: $Ce^{3+}_{0.05}$, $Eu^{2+}_{0.15}$ and BSON: $Eu^{2+}_{0.15}$, $P^{5+}_{0.09}$ further demonstrates the appearance of the Ba, Si, O, N, Ce, Eu, P elements in the studied samples (Fig. 2c and d). The results are consistent with the previous XRD results, which further confirms the formation of pure $Ba_3Si_6O_{12}N_2$ phase.

The photoluminescence properties of Ce^{3+} and Eu^{2+} monodoped BSON phosphors and energy transfer behaviour in Ce^{3+}, Eu^{2+}-codoped BSON phosphors are investigated through their photoluminescence excitation (PLE) and photoluminescence emission (PL) spectra. Fig. 3a shows the typical PLE and PL spectra of BSON: $Ce^{3+}_{0.05}$ (blue line) and BSON: $Eu^{2+}_{0.15}$ (green line) samples. It can be observed that BSON: $Eu^{2+}_{0.15}$ possesses a broad absorption band from 250 nm to 480 nm, especially presents almost equal excitation intensity between 350 nm and 460 nm, which could match well with the near ultraviolet (n-UV) and blue LED chips. Upon exciting with the 420 nm UV lamp, the BSON: $Eu^{2+}_{0.15}$ gives bright green emission, whose PL spectrum consists of a broad band from 450 nm to 650 nm centered at 520 nm due to the typical 4f [6]5 $d^1 \rightarrow 4f^7$ transition of Eu^{2+} ions [51]. The doping concentration of Ce^{3+} in BSON has been optimized to be 5 atom% Ba^{2+}. For BSON: $Ce^{3+}_{0.05}$ sample, its PLE spectrum exhibits two bands from 275 nm to 375 nm with two centers at 292 nm (the weak one) and 338 nm (the strong one), respectively. Under the excitation of 338 nm UV,

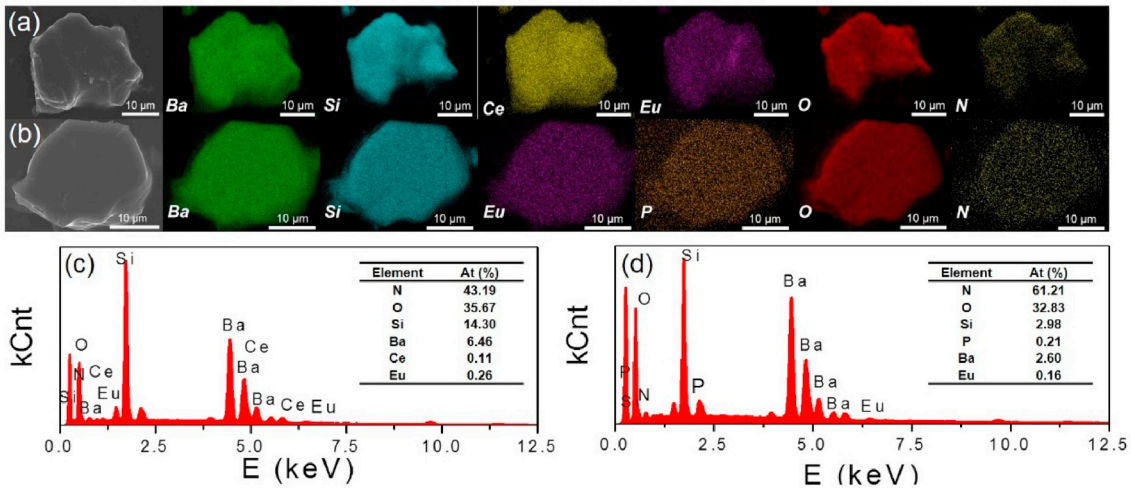

Fig. 2. SEM and EDX mapping analysis images of the representative (a) BSON: $Ce^{3+}_{0.05}$, $Eu^{2+}_{0.15}$ and BSON: $Eu^{2+}_{0.15}$, $P^{5+}_{0.09}$ samples. The EDS data and element content analysis of (a) BSON: $Ce^{3+}_{0.05}$, $Eu^{2+}_{0.15}$ and BSON: $Eu^{2+}_{0.15}$, $P^{5+}_{0.09}$ samples.

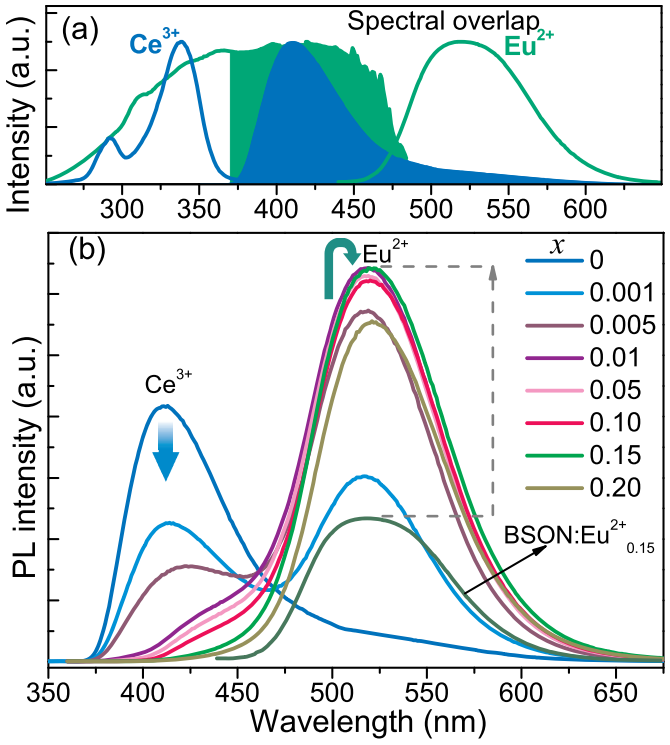

Fig. 3. (a) Typical PLE and PL spectra of BSON: $Ce^{3+}_{0.05}$ (blue line) and BSON: $Eu^{2+}_{0.15}$ (green line) samples. A completely spectral overlap between the PL spectrum of Ce^{3+} ions and PLE spectrum of Eu^{2+} ions in the $Ba_3Si_6O_{12}N_2$ host. (b) The PL spectra of BSON: $Eu^{2+}_{0.15}$, and $Ba_{2.95-x}Ce_{0.05}Eu_xSi_6O_{12}N_2$ (BSON: $Ce^{3+}_{0.05}$, Eu^{2+}_x, x = 0–0.20) samples as a function of Eu^{2+} doping concentrations (x).

BSON: $Ce^{3+}_{0.05}$ shows a strong blue emission, and the corresponding emission spectrum covers a range of 375–550 nm with the maximum emission at 420 nm. This typical blue emission should be ascribed to 5 d^1-$4f^1$ transition of Ce^{3+}. It is noted that there is an almost perfect overlapping between the PL spectrum of Ce^{3+} ions and the PLE spectrum of Eu^{2+} ions in the BSON matrix. Therefore, an efficient energy transfer could be expected from Ce^{3+} to Eu^{2+} to enhance the green emission. To determine the existence of Ce^{3+}→Eu^{2+} energy transfer, the PL spectra of BSON: $Ce^{3+}_{0.05}$, Eu^{2+}_x (x = 0–0.20) samples as a function of Eu^{2+} doping concentrations (x) are collected and plotted in Fig. 3b. The corresponding emission intensity variation of Ce^{3+} and Eu^{2+} with x values are depicted in Fig. 4a. Although the Ce^{3+}-doping concentration is fixed at 5 atom% of Ba^{2+} ions, its emission intensity gradually decrease with the increase of Eu^{2+}-doping level. Especially, at x = 15 atom% of Ba^{2+} ions, the Ce^{3+} emission completely vanish and the Eu^{2+} emission reach a maximum. Beyond x ≥ 15 atom%, the Eu^{2+} emission present a decrease due to the concentration quenching effect. The above results confirm the appearance of energy transfer between Ce^{3+} and Eu^{2+} in BSON host, and also imply an ultra-high energy transfer efficiency. To further verify the Ce^{3+}→Eu^{2+} energy transfer, the photoluminescence decay curves of BSON: $Ce^{3+}_{0.05}$, Eu^{2+}_x are measured, as shown in Fig. 4b. Since there are two Ce^{3+} emission centers in the BSON host, the decay curves could be successfully fitted using the following two-exponential equation [21]:

$$I_t = I_0 + A_1 \exp(t/\tau_1) + A_2 \exp(t/\tau_2) \quad (1)$$

where I_t and I_0 are the luminescence intensities at time t and the background intensity, respectively; A_1 and A_2 are fitting constants; and τ_1 and τ_2 are the decay times of the exponential components. Using these parameters, the average decay times (τ^*) can be determined by the formula as follows [21]:

$$\tau^* = (A_1\tau_1^2 + A_2\tau_2^2)/(A_1\tau_1 + A_2\tau_2) \quad (2)$$

When monitoring the Ce^{3+} emission at 420 nm, the calculated average decay lifetimes for the representative x = 0, 0.01, 0.05, 0.10, 0.20 samples are 36.4 ns, 30.8 ns, 19.8 ns, 17.9 ns and 14.1 ns, respectively. Obviously, the lifetime values of BSON: $Ce^{3+}_{0.05}$, Eu^{2+}_x samples monotonically decrease with increasing the Eu^{2+}-doping concentration. This is a definite evidence to confirm the existence of Ce^{3+}→Eu^{2+} energy transfer. The energy transfer efficiency from Ce^{3+} to Eu^{2+} in BSON can be determined by the following equation [52]:

$$\eta_T = 1 - \tau_S/\tau_{S0} \quad (3)$$

where η_T is the energy transfer efficiency and τ_{S0} and τ_S are the decay lifetimes of Ce^{3+} in the absence and presence of Eu^{2+}, respectively. Fig. 4c shows the results of energy transfer efficiency (η_T) from Ce^{3+} to Eu^{2+} calculated using Eq. (3). It is clearly seen that the energy transfer efficiency gradually increases with increasing Eu^{2+} concentration without appearing a saturation behaviour. The maximum energy transfer efficiency reaches 100%, indicating a complete energy transfer from Ce^{3+} to Eu^{2+} in the BSON matrix, which is firstly observed in rare earth doped oxonitridosilicates. Based on the Ce^{3+}→Eu^{2+} energy transfer, the emission intensity of BSON: $Ce^{3+}_{0.05}$, $Eu^{2+}_{0.15}$ is obviously

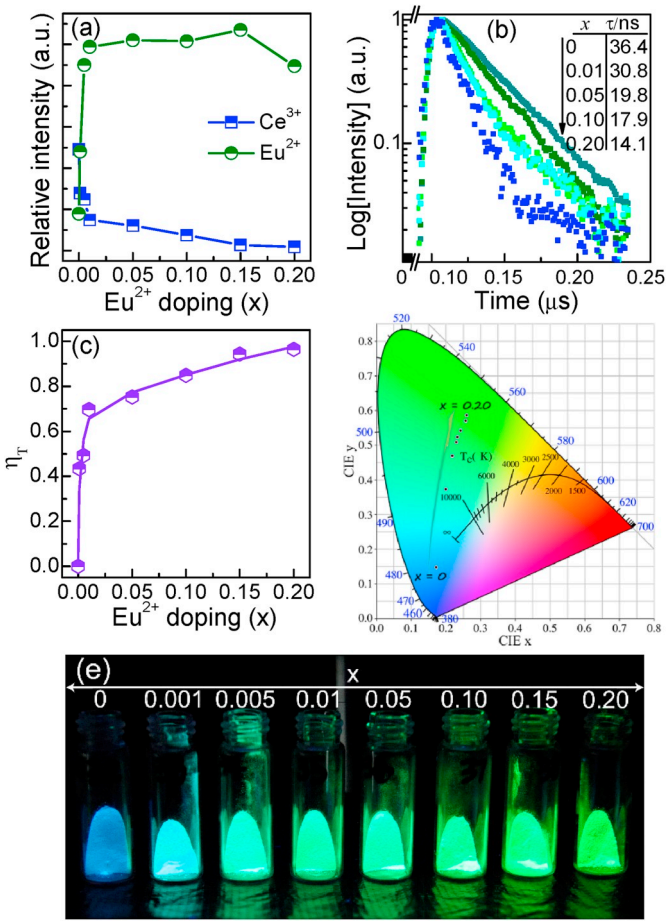

Fig. 4. (a) The integrated emission intensity of BSON: $Ce^{3+}_{0.05}$, Eu^{2+}_{x} samples with Eu^{2+}-doping (x). (b) The luminescence decay curves of BSON: $Ce^{3+}_{0.05}$, Eu^{2+}_{x} with x values with the emission monitoring wavelength at 420 nm. (c) The energy transfer efficiency of BSON: $Ce^{3+}_{0.05}$, Eu^{2+}_{x} (x = 0–0.20) samples with the increase of x. (d) The CIE color coordinates and (e) corresponding luminescence photos (inserts, under 365 nm UV lamp) of BSON: $Ce^{3+}_{0.05}$, Eu^{2+}_{x} (x = 0–0.20) samples.

improved relative to the BSON: $Eu^{2+}_{0.15}$, which is about 2.5 times than that of the latter (Fig. 3b). The corresponding quantum yields in Table 4 also confirm the above result, which is enhanced from 79% (BSON: $Eu^{2+}_{0.15}$) to 88% (BSON: $Ce^{3+}_{0.05}$, $Eu^{2+}_{0.15}$). Except for the improvement of emission intensity, a wider range of luminescence control has been acquired in BSON: $Ce^{3+}_{0.05}$, Eu^{2+}_{x}. As shown in Fig. 4d and Table 4, the CIE color coordinate points of the studied samples gradually shift from blue region (0.173, 0.148) to green region (0.259, 0.586) through simply changing the Eu^{2+}-doping concentration. The corresponding luminescence photos intuitively demonstrate the controllable luminescence variation between blue and green (Fig. 4e).

It is pointed out that after x > 15 atom%, the Eu^{2+} emission show a sharp decrease, which is attributed to the concentration quenching effect. Usually, the distance between emission center ions becomes shorter at a high doping level. Then energy migration more easily happens among the activator ions and reaches a quenching center, and finally results in the luminescence quenching. The critical distance R_C for energy transfer from Ce^{3+} to Eu^{2+} in BSON host can be estimated using the equation given by Blasse [53]:

$$R_c \approx 2\left[\frac{3V}{4\Pi \times N}\right]^{1/3} \quad (4)$$

where V is the volume of the unit cell, X_c is the critical concentration of Ce^{3+} and Eu^{2+} ions, and N is the number of host cations in the unit cell.

Table 4
The CIE color coordinates, quantum yield and emission peaks of BSON: $Ce^{3+}_{0.05}$, Eu^{2+}_{x} samples (λ_{ex} = 420 nm) and BSON: $Eu^{2+}_{0.15}$, P^{5+}_{y} samples (λ_{ex} = 420 nm, 460 nm).

No.	Samples	CIE (x, y) λ_{ex} = 420 nm		Quantum yield (%)	Peak (nm)
1	BSON:$Ce^{3+}_{0.05}$	(0.173, 0.148)		57	413
2	BSON: $Eu^{2+}_{0.15}$	(0.278, 0.609)		64	519
3	BSON:$Ce^{3+}_{0.05}$, $Eu^{2+}_{0.001}$	(0.199, 0.373)		65	517
4	BSON:$Ce^{3+}_{0.05}$, $Eu^{2+}_{0.005}$	(0.219, 0.470)		67	519
5	BSON:$Ce^{3+}_{0.05}$, $Eu^{2+}_{0.01}$	(0.231, 0.510)		70	519
6	BSON:$Ce^{3+}_{0.05}$, $Eu^{2+}_{0.05}$	(0.234, 0.524)		72	519
7	BSON:$Ce^{3+}_{0.05}$, $Eu^{2+}_{0.10}$	(0.243, 0.543)		76	520
8	BSON:$Ce^{3+}_{0.05}$, $Eu^{2+}_{0.15}$	(0.259, 0.571)		82	519
9	BSON:$Ce^{3+}_{0.05}$, $Eu^{2+}_{0.20}$	(0.259, 0.586)		72	521
		λ_{ex} = 420 nm	λ_{ex} = 460 nm		
10	BSON: $Eu^{2+}_{0.15}$, $P^{5+}_{0.01}$	(0.288, 0.581)	(0.283, 0.604)	68	519
11	BSON: $Eu^{2+}_{0.15}$, $P^{5+}_{0.05}$	(0.293, 0.574)	(0.282, 0.606)	69	520
12	BSON: $Eu^{2+}_{0.15}$, $P^{5+}_{0.09}$	(0.289, 0.577)	(0.285, 0.604)	75	520
13	BSON: $Eu^{2+}_{0.15}$, $P^{5+}_{0.15}$	(0.290, 0.575)	(0.277, 0.610)	70	519

In this case, $N = 1$, $V = 310.03$ Å^3, and the critical doping concentrations of Ce^{3+} and Eu^{2+} in the BSON host is 6.7 atom% of Ba^{2+}. Therefore, the critical distance (R_C) was calculated to be about 20.7 Å. For the resonant energy-transfer mechanism, the multipolar interaction plays an important role when R_C locates in 4–27 Å [54]. Thus, the electric multipolar interaction is responsible for energy transfer between the Ce^{3+} and Eu^{2+} ions in the BSON host. The radiative emission from Eu^{2+} prevails when $R_{Ce\text{-}Eu} > R_C$, and in reverse the energy transfer from Ce^{3+} to Eu^{2+} dominates. According to Dexter's energy transfer formula of multipolar interaction and Reisfeld' s approximation, the relationship can be expressed [55]:

$$\eta_{SO} / \eta_S \propto x^{n/3} \quad (5)$$

where x is the sum of Eu^{2+} content; η_{SO} and η_S are the luminescence quantum efficiency of Ce^{3+} in the absence and presence of Eu^{2+}, $n = 6$, 8, and 10 corresponding to dipole−dipole, dipole−quadrupole, and quadrupole−quadrupole interactions, respectively. The value η_{SO} / η_S is approximately calculated by the ratio of relative emission intensities as [56]:

$$I_{SO} / I_S \propto x^{n/3} \quad (6)$$

where I_{SO} is the intrinsic luminescence intensity of Ce^{3+}, and I_S is the luminescence intensity of Ce^{3+} in the presence of the Eu^{2+}. The relationships between I_{SO}/I_S and $x^{n/3}$ are plotted in Fig. 5a−5d. The optimal linear relationship for $I_{SO}/I_S \propto x^{8/3}$ by comparing the fitting factors of R^2 values is at $n = 8$. Therefore, the energy transfer mechanism from Ce^{3+} to Eu^{2+} ions in BSON host is determined to be the electric dipole−quadrupole interaction [54].

For pc-WLEDs lighting source, the green emission component has a more contribution to luminescence efficiency compared with another spectral component such as blue light and red light [20–25]. Accordingly, in order to enhance the luminous efficiency of WLEDs devices, it is necessary to further optimize and improve the luminescence performances of some current green-emitting phosphors. It is well known that

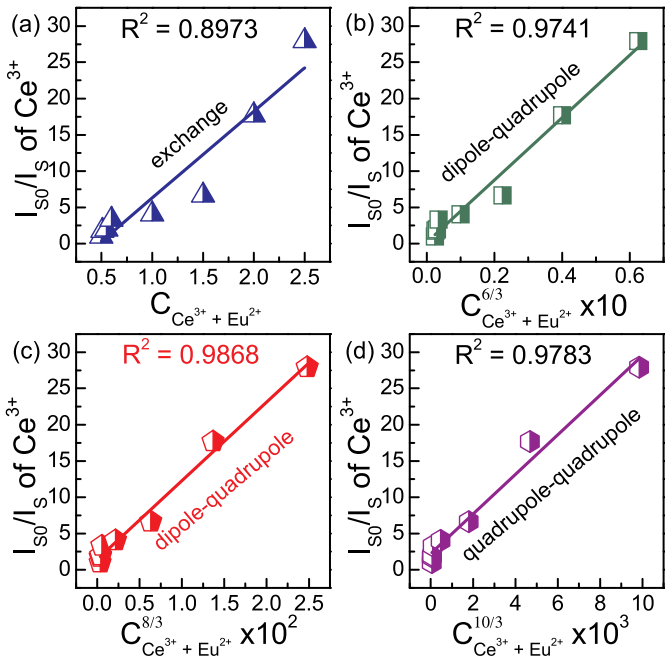

Fig. 5. Dependence of I_{S0}/I_S of Ce^{3+} ions on (a) C_{Ce+Eu}, (b) $C_{Ce+Eu} \times 10$, (c) $C_{Ce+Eu} \times 10^2$ and (d) $C_{Ce+Eu} \times 10^3$ in BSON: $Ce^{3+}{}_{0.05}$, $Eu^{2+}{}_x$ (x = 0–0.20) system.

the $Ba_3Si_6O_{12}N_6$:Eu^{2+} has been extensively reported as highly efficient green emitting phosphor for WLEDs [47–51]. To further promote the commercialization of $Ba_3Si_6O_{12}N_6$:Eu^{2+} green phosphor, the luminescence performances including the spectral profile, quantum yield and thermal stability need be further improved and optimized. Fig. 6a and b plots PLE and PL spectra of BSON: $Eu^{2+}{}_{0.15}$ (light green line) and BSON: $Eu^{2+}{}_{0.15}$, $P^{5+}{}_{0.09}$ (dark green line) sample monitoring at different emission and excitation wavelengths, respectively. Although monitoring at different emission wavelengths, the above two samples almost present the exactly same PLE spectra profiles. For BSON: $Eu^{2+}{}_{0.15}$ sample, the PL spectra are completely same with the fwhm about 80 nm upon exciting with 420 nm and 460 nm. When radiating under different excitation wavelengths, BSON: $Eu^{2+}{}_{0.15}$, $P^{5+}{}_{0.09}$ presents an obvious widening in the fwhms of PL spectra that reaches 98 nm (λ_{ex} = 460 nm) and 102 nm (λ_{ex} = 420 nm). Moreover, there are evident two emission peaks could be observed at 502 nm and 545 nm. As shown in Fig. 6c, the fwhms of BSON: $Eu^{2+}{}_{0.15}$, $P^{5+}{}_y$ samples gradually enlarge with the doping of P^{5+} ions. This widening in PL spectra possibly originate from the lattice distortion in local region with the introduction of P^{5+} ions due to the different ion radius between Si^{4+} ion and P^{5+} ion. The luminescence decay curves of BSON: $Eu^{2+}{}_{0.15}$, $P^{5+}{}_{0.09}$ demonstrate a gradually increasing lifetime values 1.26, 1.36, 1.43 μs monitoring at different emission wavelengths 507, 520, 539 nm, respectively. This result further confirms that different emission centers appear after doping the P^{5+} ion into BSON host. However, BSON: $Eu^{2+}{}_{0.15}$, $P^{5+}{}_{0.09}$ maintains a pure trigonal phase of $Ba_3Si_6O_{12}N_2$, as presented in Fig. 1a. Therefore, the different emission centers that results in the widening PL spectra should be attributed to local lattice distortion or small nanophase mixing of $BaSi_2O_2N_2$, which is consistent with the previous report.

Interestingly, the emission intensity of BSON: $Eu^{2+}{}_{0.15}$, $P^{5+}{}_y$ samples with P^{5+} doping (y) present a trend of rising first and then falling, reaching a maximum at y = 0.09 (under 420 and 460 nm excitation) (Fig. 6d). For the luminescence improvement at $0 < y \leq 0.09$ in the studied system, two main reasons could be suggested. The first reason is that the Ba^{2+} ions are larger than Eu^{2+} ions at the same coordination situation, and thus the replacement of Eu^{2+} for Ba^{2+} will generate the lattice expansion and distortion. After introducing P^{5+} ions into BSON

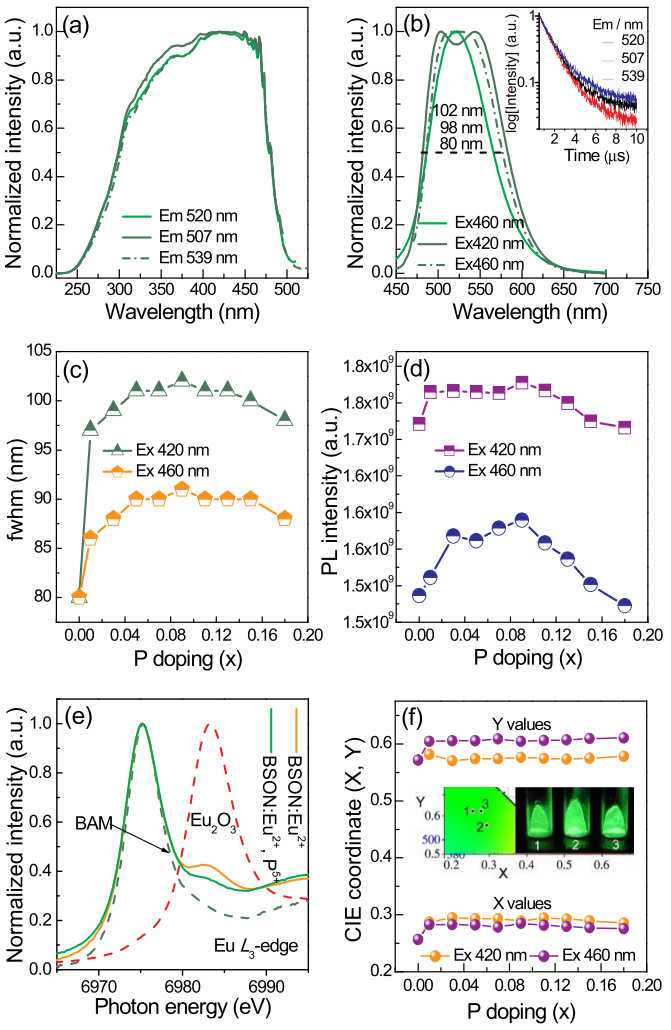

Fig. 6. (a) PLE and (b) PL spectra of BSON: $Eu^{2+}{}_{0.15}$ (light green line) and BSON: $Eu^{2+}{}_{0.15}$, $P^{5+}{}_{0.09}$ (dark green line) sample monitoring at different emission and excitation wavelengths, respectively. The insert in (b) is the luminescence decay curves of BSON: $Eu^{2+}{}_{0.15}$, $P^{5+}{}_{0.09}$ monitoring at different emission wavelengths (507, 520 and 539 nm; 1.26, 1.36 and 1.43 μs). (c) The integrated emission intensity and (d) the emission fwhm of BSON: $Eu^{2+}{}_{0.15}$, $P^{5+}{}_y$ samples with P^{5+} doping (y) (λ_{ex} = 420 and 460 nm). (e) Normalized Eu L_3-edge X-ray absorption near edge structure (XANES) spectra of BSON: $Eu^{2+}{}_{0.15}$ and BSON: $Eu^{2+}{}_{0.15}$, $P^{5+}{}_{0.09}$ samples. The normalized XANES data of standard BAM and Eu_2O_3 samples are shown as references. (f) The CIE color coordinates of BSON: $Eu^{2+}{}_{0.15}$, $P^{5+}{}_y$ samples (λ_{ex} = 420 and 460 nm). "1–3″represent the color coordinates and luminescence photos of BSON: $Eu^{2+}{}_{0.15}$ [(0.278, 0.609), λ_{ex} = 420 and 460 nm] and BSON: $Eu^{2+}{}_{0.15}$, $P^{5+}{}_{0.09}$ [(0.289, 0.577), λ_{ex} = 420 nm; (0.285, 0.604), λ_{ex} = 460 nm].

host, the lattice shrinkage and the relax of lattice strain could be expected due to the obviously smaller radii of P^{5+} ions than Si^{4+} ions, which results in the increase of lattice rigidity. Another one is that the increase of the PL intensity should originate from the decrease of Eu^{3+} ions in BSON: $Eu^{2+}{}_{0.15}$, $P^{5+}{}_y$ samples with the doping of P^{5+} ions. Although the Eu^{2+}-activated phosphors are usually prepared under a reducing atmosphere, Eu^{3+} will inevitably coexist in the host lattice. In the current system, the charge mismatch of P^{5+} and Si^{4+} easily forms positive charge defects in this host. To keep a charge-balance, part of the Eu^{3+} ions is reduced to Eu^{2+} with the doping of P^{5+} ions. In view of the different threshold energies of Eu^{2+} ($4f^7$) and Eu^{3+} ($4f^6$) to 5*d* states, X-ray absorption near edge structure (XANES) spectra could be utilized to determine the valence of the Eu element [58,59].

Owing to the stronger shielding effect of nuclear potential, the Eu^{2+}

exhibits the lower binding energy than that of Eu^{3+} [57–60]. Fig. 6e shows the normalized Eu L_3-edge X-ray absorption near edge structure (XANES) spectra of BSON: $Eu^{2+}_{0.15}$ and BSON: $Eu^{2+}_{0.15}$, $P^{5+}_{0.09}$ samples. The XANES spectra of standard BAM ($BaMgAl_{10}O_{17}:Eu^{2+}$) and Eu_2O_3 samples are shown as references. Obviously, two peaks at 6974 and 6983 eV are observed, which are attributed to the electron transitions of $2p_{3/2}$-5d in Eu^{2+} and Eu^{3+}, respectively. It is noticed that the 6983 eV peak of P^{5+}-doped BSON: $Eu^{2+}_{0.15}$, $P^{5+}_{0.09}$ is slightly lower than that of BSON: $Eu^{2+}_{0.15}$, implying a decrease content of Eu^{3+} ions in BSON: $Eu^{2+}_{0.15}$, $P^{5+}_{0.09}$. Accordingly, the PL intensity of BSON: $Eu^{2+}_{0.15}$, $P^{5+}_{0.09}$ is enhanced relative to P^{5+}-undoped sample.

The luminescence quenching beyond $y > 0.09$ should be ascribed to excessive positive charge defects due to the unbalanced substitution of P^{5+} ions for Si^{4+} ions, which enhances the nonradiative transition. Finally, the CIE color coordinates and luminescence photos of BSON: $Eu^{2+}_{0.15}$, P^{5+}_{y} samples (under 420 and 460 nm excitation) are collected in Fig. 6f and Table 4. The CIE color coordinate position for BSON: $Eu^{2+}_{0.15}$ [(0.278, 0.609), λ_{ex} = 420 and 460 nm] and BSON: $Eu^{2+}_{0.15}$, $P^{5+}_{0.09}$ [(0.289, 0.577), λ_{ex} = 420 nm; (0.285, 0.604), λ_{ex} = 460 nm] generate an obvious shift as monitoring at different excitation wavelengths, as given in Fig. 6f. The result is consistent with the PL results in Fig. 6b, and also confirm the widening of PL spectra with the doping of P^{5+} ions.

For a practical WLEDs device, thermal stability of phosphors is a key indicator to realize high-quality white lighting [61–63]. The temperature-dependent luminescence properties of the studied samples need to be discussed. Fig. 7a give the temperature-dependent PL spectra of BSON: $Eu^{2+}_{0.15}$ with a range of 25–250 °C. Unsurprisingly, It could be clearly observed that the emission intensity of BSON: $Eu^{2+}_{0.15}$ sample decreases clearly with increasing temperature from 25 to 250 °C because of nonradiative transitions, which could retain 80% of the original value at 150 °C. Moreover, a blue-shifted emission about 12 nm is observed with increasing the working temperatures. Fig. 7b depicts the shift rate of emission peaks and the decreasing rate of emission intensity of Eu^{2+} at two different luminescence centers (Ba1 and Ba2) with a range of 25–250 °C. By comparing the Gaussian fitting spectra of BSON: $Eu^{2+}_{0.15}$ decomposed from Ba1 sites and Ba2 sites, it is found that the Ba2 emission intensity (low-energy emission) presents a faster decline rate than Ba1 emission (high-energy emission). The above results make the Ba2 emission peaks ($k_2 = -0.032$) generate a faster shift rate than Ba1 emission peaks ($k_1 = -0.028$), and finally results in a blue shift. Therefore, this blue shift emission with temperatures in BSON: $Eu^{2+}_{0.15}$ should mainly result from the lattice variation surrounding activator ions at different lattice sites [64–66]. Interestingly, the P^{5+}-doped

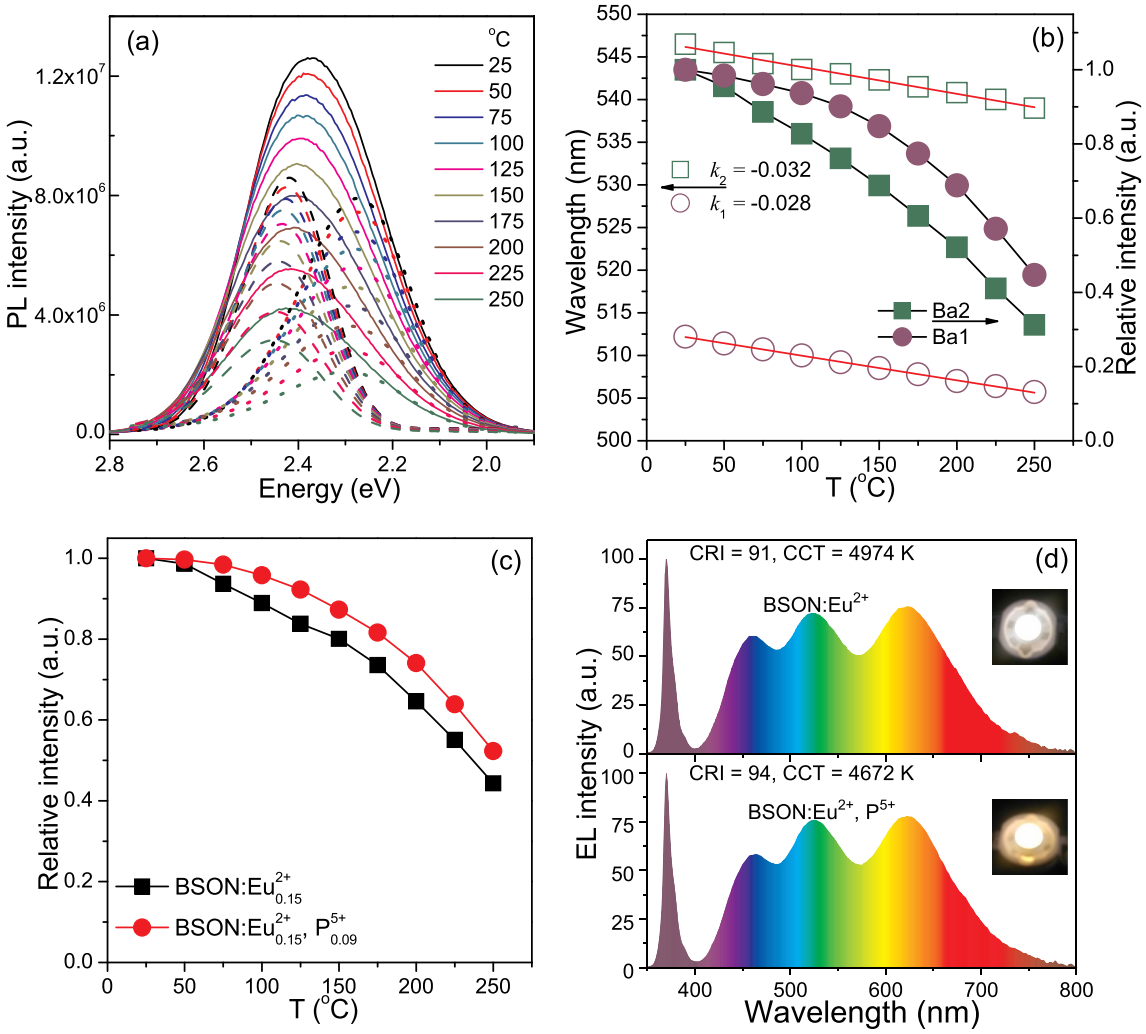

Fig. 7. (a) Temperature-dependent PL spectra and corresponding Gaussian fitting PL spectra of BSON: $Eu^{2+}_{0.15}$ with a range of 25°C–250 °C. (b) The change of emission wavelength and relative intensity of Eu^{2+} at two different luminescence centers (Ba1 and Ba2) with a range of 25–250 °C. (c) Temperature-dependent relative integral intensity of BSON: $Eu^{2+}_{0.15}$ and BSON: $Eu^{2+}_{0.15}$, P^{5+}_{y} samples (25–250 °C). (d) The electroluminescence spectra of WLEDs devices fabricated with BSON: Eu^{2+} and BSON: Eu^{2+}, P^{5+} phosphors and commercial blue BAM phosphor and red $CaAlSiN_3:Eu^{2+}$ phosphor. The insets are the corresponding luminescence photos.

sample exhibit a better thermal stability than that of BSON: $Eu^{2+}_{0.15}$. The emission intensity of BSON: $Eu^{2+}_{0.15}$, $P^{5+}_{0.09}$ at 423 K still maintain 88% of the room-temperature emission intensity, which is enhanced 8% than pure BSON: $Eu^{2+}_{0.15}$ (Fig. 7c). Moreover, the stability could be further improved by optimizing synthesis condition.

The possible improvement mechanism is that the introduction of P^{5+} ions into BSON: $Eu^{2+}_{0.15}$ release the lattice strain and distortion induced by the mismatch of ion radius between Eu^{2+} ions and Ba^{2+} ions, and simultaneously increase the lattice rigidity. In addition, the enhanced crystallinity with the P^{5+}-doping also contributes the thermal stability improvement. Finally, to evaluate the device performance of the as-prepared BSON: $Eu^{2+}_{0.15}$, P^{5+}_{x} phosphors, we fabricated white LEDs with UV chip (370 nm) and blue BAM, green BSON: $Eu^{2+}_{0.15}$ and BSON: $Eu^{2+}_{0.15}$, $P^{5+}_{0.09}$ as well as $CaAlSiN_3:Eu^{2+}$ phosphors. The electroluminescence (EL) spectra are shown in Fig. 7d. Under a voltage of 3.15 V and bias current of 20 mA, the warm white with low corresponding color temperature (CCT = 4672 K), high color rendering index (R_a = 94) has been achieved, which shows a lower CCT and higher R_a than that of BSON: $Eu^{2+}_{0.15}$ phosphor (CCT = 4974 K, R_a = 91). These results suggest that the as-prepared BSON: $Eu^{2+}_{0.15}$, $P^{5+}_{0.09}$ could be an excellent candidate for a green-emitting phosphor material for better application in near-UV chip based WLEDs.

4. Conclusions

In summary, a series of Ce^{3+} and P^{5+}-doped $Ba_3Si_6O_{12}N_2:Eu^{2+}$ green phosphors were successfully prepared by a traditional high-temperature solid state reaction. According to the Rietveld refinement results, the as-synthesized phosphors all crystallized into trigonal phase (*P*-3) of $Ba_3Si_6O_{12}N_2$. Ce^{3+}, Eu^{2+} and P^{5+} ions mainly occupy the Ba^{2+} sites and Si^{4+} sites, respectively. Moreover, Ce^{3+} and Eu^{2+} ions randomly occupy two Ba crystallographic sites (Ba1 and Ba2). For Ce^{3+} and Eu^{2+} mono-doped samples, it shows blue emission (~420 nm) and green emission (~520 nm), respectively. Interestingly, an almost complete spectral overlap between Ce^{3+} emission and Eu^{2+} excitation has been observed in BSON matrix. Thence, a near unity energy transfer (~100%) from Ce^{3+} to Eu^{2+} is realized and the corresponding mechanism is determined to be dipole-quadrupole electrical multipole interactions. Based on the complete $Ce^{3+}\rightarrow Eu^{2+}$ ET, the luminescence intensity of BSON: Ce^{3+}, Eu^{2+} is obviously enhanced, which reaches about 2.5 times of BSON: Eu^{2+}. Furthermore, a broad color tuning from blue (0.173, 0.148) to green (0.259, 0.571) has been achieved. In addition, the P^{5+}-doping also help improve the luminescence emission. The Eu L_3-edge XANES spectra indicate that the emission improvement should be attributed the transformation from Eu^{3+} to Eu^{2+} with the P^{5+}-doping due to the $[Eu^{3+}$-$Si^{4+}]\rightarrow[Eu^{2+}$-$P^{5+}]$ charge compensation mechanism. It is noticed that the thermal stability of BSON: Eu^{2+} is also slightly improved. The emission intensity of BSON: $Eu^{2+}_{0.15}$, $P^{5+}_{0.09}$ at 423 K still maintain 88% of the room-temperature emission intensity, which is enhanced 8% than pure BSON: $Eu^{2+}_{0.15}$. The possible reason is the increase of lattice rigidity and the relax of lattice strain caused by the mismatched substitution of Eu^{2+} for Ba^{2+}. Finally, the WLEDs fabricated by combining the presentative P^{5+}-doped BSON: Eu^{2+}, BAM and CASN phosphors present a lower CCT (4672 K) and higher Ra (94) than that of employing BSON: Eu^{2+}, suggesting that the as-prepared Ce^{3+}/P^{5+}-codoped $Ba_3Si_6O_{12}N_2:Eu^{2+}$ could be an excellent green-emitting phosphor material for application in UV-to-visible based WLEDs.

Declaration of competing interest

There are no conflicts to declare.Conflict of interest statement. We declare that we have no financial and personal relationships with other people or organizations that can inappropriately influence our work, there is no professional or other personal interest of any nature or kind in any product, service and/or company that could be construed as influencing the position presented in, or the review of, the manuscript entitled.

CRediT authorship contribution statement

Jiarui Hao: Formal analysis, Writing - original draft. **Mengxuan Tao:** Data curation. **Zhiyu Gao:** Data curation. **Shuoting Chen:** Investigation. **Yixin Liu:** Investigation. **Hongquan Wang:** Investigation. **Yi Wei:** Data curation. **Maxim S. Molokeev:** Data curation. **Guogang Li:** Writing - review & editing, Funding acquisition.

Acknowledgements

This work is financially supported by the National Natural Science Foundation of China (NSFC No. 51672259, 51601131) and the Fundamental Research Fund for National Universities, China University of Geosciences (Wuhan).

Appendix A. Supplementary data

Supplementary data to this article can be found online at https://doi.org/10.1016/j.jlumin.2019.116995.

References

[1] X. Qin, X. Liu, W. Huang, M. Bettinelli, X. Liu, Chem. Rev. 117 (2017) 4488–4527.
[2] C.C. Lin, R.S. Liu, J. Phys. Chem. Lett. 2 (2011) 1268–1277.
[3] Z.G. Xia, Q.L. Liu, Prog. Mater. Sci. 84 (2016) 59–117.
[4] P.P. Dai, C. Li, X.T. Zhang, J. Xu, X. Chen, X.L. Wang, Y. Jia, X.J. Wang, Y.C. Liu, Light Sci. Appl. 5 (2016), e16024.
[5] M.H. Fang, S. Mahlik, A. Lazarowska, M. Grinberg, M.S. Molokeev, H.S. Sheu, J. F. Lee, R.S. Liu, Angew. Chem. Int. Ed. 58 (2019) 7767–7772.
[6] J.W. Lee, S.P. Singh, M. Kim, S.U. Hong, W.B. Park, K.S. Sohn, Inorg. Chem. 56 (2017) 9814–9824.
[7] J. Ueda, P. Dorenbos, A.J.J. Bos, A. Meijerink, S. Tanabe, J. Phys. Chem. C 119 (2015) 25003–25008.
[8] P. Strobel, V. Weiler, P.J. Schmidt, W. Schnick, Chem. 24 (2018) 7243–7249.
[9] T. Senden, R.J.A. van Dijk–Moes, A. Meijerink, Light Sci. Appl. 7 (2018) 8.
[10] L. Yin, Y. Liang, S. Zhang, M. Wang, L. Li, W. Xie, H. Zhong, X. Jian, X. Xu, X. Wang, L. Deng, Chem. Commun. 54 (2018) 3480–3483.
[11] H. Chen, C. Cai, Z. Zhang, L. Zhang, H. Lu, X. Xu, H. Bui, K. Qiu, L. Yin, J. Alloy. Comp. 801 (2019) 10–18.
[12] S. Zhang, H. Chen, C. Cai, Z. Zhang, Y. Zhao, L. Zhang, X. Wang, L. Zhang, X. Xu, H. Bui, L. Yin, J. Alloy. Comp. 799 (2019) 360–367.
[13] N. Hirosaki, R.J. Xie, K. Kimoto, T. Sekiguchi, Y. Yamamoto, T. Suehiro, M. Mitomo, Appl. Phys. Lett. 86 (2005) 211905.
[14] F.W. Kang, H.S. Zhang, L. Wondraczek, X.B. Yang, Y. Zhang, D.Y. Lei, M.Y. Peng, Chem. Mater. 28 (2016) 2692–2703.
[15] X.J. Zhang, H.–C. Wang, A.–C. Tang, S.–Y. Lin, H.–C. Tong, C.–Y. Chen, Y.–C. Lee, T.–L. Tsai, R.–S. Liu, Chem. Mater. 28 (2016) 8493–8497.
[16] L. Wang, R.–J. Xie, T. Suehiro, T. Takeda, N. Hirosaki, Chem. Rev. 118 (2018) 1951–2009.
[17] Y. Xiao, W.G. Xiao, L.L. Zhang, Z.D. Hao, G.H. Pan, Y. Yang, X. Zhang, J.H. Zhang, J. Mater. Chem. C 6 (2018) 12159–12163.
[18] J. Ma, H. Wu, J.B. Qiu, J. Wang, Q. Wang, Y. Yang, D.C. Zhou, J. Han, J. Mater. Chem. C 7 (2019) 3751–3755.
[19] Q.S. Wu, Z.G. Yang, Z.Y. Zhao, M.D. Que, X.C. Wang, Y.H. Wang, J. Mater. Chem. C 2 (2014) 4967–4973.
[20] M.Y. Wang, X. Zhang, Z.D. Hao, X.G. Ren, Y.S. Luo, X.J. Wang, J.H. Zhang, Opt. Mater. 32 (2010) 1042–1045.
[21] C.X. Li, H. Chen, Y.J. Hua, L.L. Yu, Q.Y. Jiang, D.G. Deng, S.L. Zhao, H.P. Ma, S. Q. Xu, Opt. Commun. 295 (2013) 129–133.
[22] M. Seibald, T. Rosenthal, O. Oeckler, W. Schmick, Crit. Rev. Solid State 39 (2014) 215–229.
[23] X.C. Wang, T. Seto, Z.Y. Zhao, Y.Y. Li, Q.S. Wu, H. Li, Y.H. Wang, J. Mater. Chem. C 2 (2014) 4476–4481.
[24] S.X. Li, L. Wang, D.M. Tang, Y.J. Cho, X.J. Liu, X.T. Zhou, L. Lu, L. Zhang, T. Takeda, N. Hirosaki, R.–J. Xie, Chem. Mater. 30 (2018) 494–505.
[25] J.Y. Zhong, W.R. Zhao, F. Du, J. Wen, W.D. Zhuang, R.H. Liu, C.–K. Duan, L. G. Wang, K. Lin, J. Phys. Chem. C 122 (2018) 7849–7858.
[26] G.G. Li, Y. Tian, Y. Zhao, J. Lin, Chem. Soc. Rev. 44 (2015) 8688–8713.
[27] Z.Y. Zhao, Z.G. Yang, Y.R. Shi, C. Wang, B.T. Liu, G. Zhu, Y.H. Wang, J. Mater. Chem. C 1 (2013) 1407–1412.
[28] S.S. Wang, W.T. Che, Y. Li, J. Wang, H.S. Sheu, R.S. Liu, J. Am. Chem. Soc. 135 (2013) 12504–12507.
[29] W.Z. Sun, R. Pang, H.M. Li, D. Li, L.H. Jiang, S. Zhang, J.P. Fu, C.Y. Li, J. Mater. Chem. C 5 (2017) 1346–1355.
[30] H. Zhu, C.C. Lin, W. Luo, S. Shu, Z. Liu, Y. Liu, J. Kong, E. Ma, Y. Cao, R.–S. Liu, X. Chen, Nat. Commun. 5 (2014) 4312.

[31] Y.H. Kim, P. Arunkumar, B.Y. Kim, S. Unithrattil, E. Kim, S.H. Moon, J.Y. Hyun, K. H. Kim, D. Lee, J.S. Lee, W.B. Im, Nat. Mater. 16 (2017) 543–550.
[32] W.B. Park, S.P. Singh, K.S. Sohn, J. Am. Chem. Soc. 136 (2014) 2363–2373.
[33] C.C. Lin, Y.T. Tsai, H.E. Johnston, M.H. Fang, F. Yu, W. Zhou, P. Whitfield, Y. Li, J. Wang, R.S. Liu, J.P. Attfield, J. Am. Chem. Soc. 139 (2017) 11766–11770.
[34] Y. Wei, L. Cao, L. Lv, G. Li, J. Hao, J. Gao, C. Su, C.C. Lin, H.S. Jang, P. Dang, J. Lin, Chem. Mater. 30 (2018) 2389–2399.
[35] X. Piao, K.−i. Machida, T. Horikawa, H. Hanzawa, Y. Shimomura, N. Kijima, Chem. Mater. 19 (2007) 4592–4599.
[36] N.C. George, J. Brgoch, A.J. Pell, C. Cozzan, A. Jaffe, G. Dantelle, A. Llobet, G. Pintacuda, R. Seshadri, B.F. Chmelka, Chem. Mater. 29 (2017) 3538–3546.
[37] P. Strobel, C. Maak, V. Weiler, P.J. Schmidt, W. Schnick, Angew. Chem. Int. Ed. 57 (2018) 8739–8743.
[38] Y. Masubuchi, S. Nishitani, A. Hosono, Y. Kitagawa, J. Ueda, S. Tanabe, H. Yamane, M. Higuchi, S. Kikkawa, J. Mater. Chem. C 6 (2018) 6370–6377.
[39] Y. Wei, G. Xing, K. Liu, G. Li, P. Dang, S. Liang, M. Liu, Z. Cheng, D. Jin, J. Lin, Light Sci. Appl. 8 (2019) 15.
[40] Z. Tang, G. Zhang, Y. Wang, ACS Photonics 5 (2018) 3801–3813.
[41] Y. Liu, X. Zhang, Z. Hao, X. Wang, J. Zhang, Chem. Commun. 47 (2011) 10677–10679.
[42] J. Li, J. Ding, Y. Cao, X. Zhou, B. Ma, Z. Zhao, Y. Wang, ACS Appl. Mater. Interfaces 10 (2018) 37307–37315.
[43] L. Lin, L. Ning, R. Zhou, C. Jiang, M. Peng, Y. Huang, J. Chen, Y. Huang, Y. Tao, H. Liang, Inorg. Chem. 57 (2018) 7090–7096.
[44] X. Ji, J. Zhang, Y. Li, S. Liao, X. Zhang, Z. Yang, Z. Wang, Z. Qiu, W. Zhou, L. Yu, S. Lian, Chem. Mater. 30 (2018) 5137–5147.
[45] H. Terraschke, C. Wickleder, Chem. Rev. 115 (2015) 11352–11378.
[46] C. Wang, Z.Y. Zhao, Q.S. Wu, S.Y. Xin, Y.H. Wang, CrystEngComm. 16 (2014) 9651–9656.
[47] J.Y. Tang, J.H. Chen, L.Y. Hao, X. Xu, W.J. Xie, Q.X. Li, J. Lumin. 131 (2011) 1101–1106.
[48] Bruker AXS TOPAS V4, General Profile and Structure Analysis Software for Powder Diffraction data.–User's Manual, Bruker AXS, Karlsruhe, Germany, 2008.
[49] C. Braun, M. Seibald, S.L. Boerger, O. Oeckler, T.D. Boyko, A. Moewes, G. Miehe, A. Tücks, W. Schnick, Chem−Eur. J. 16 (2010) 9646–9657.
[50] T.T. Li, Y. Kotuska, T. Fukuda, T. Kurushim, N. Kamata, Mater. Lett. 145 (2015) 158–161.
[51] Y.H. Song, M.O. Kim, M.K. Jung, K. Senthil, T. Masaki, K. Toda, D.H. Yoon, Mater. Lett. 77 (2012) 121–124.
[52] N. Guo, Y.J. Huang, H.P. You, M. Yang, Y.H. Song, K. Liu, Y.H. Zheng, Inorg. Chem. 49 (2010) 10907–10913.
[53] Y. Tian, Y. Wei, Y. Zhao, Z.W. Quan, G.G. Li, J. Lin, J. Mater. Chem. C 4 (2016) 1281–1294.
[54] J.Y. Chen, N.M. Zhang, C.F. Guo, F.J. Pan, X.J. Zhou, H.S. Xiao, Q. Zhao, E. M. Goldys, ACS Appl. Mater. Interfaces 8 (2016) 20856–20864.
[55] R. Reisfeld, E. Greenberg, R. Velapoldi, B. Barnett, J. Chem. Phys. 56 (1972) 1698–1750.
[56] M.M. Jiao, Q.F. Xu, C.L. Yang, M.L. Liu, J. Mater. Chem. C 6 (2018) 4435–4443.
[57] K.W. Huang, W.T. Chen, C.I. Chu, S.F. Hu, H.S. Sheu, B.M. Cheng, J.M. Chen, R. S. Liu, Chem. Mater. 24 (2012) 2220–2227.
[58] Y.F. Xia, J. Chen, Y.G. Liu, M.S. Molokeev, M. Guan, Z.H. Huang, M.H. Fang, Dalton Trans. 45 (2016) 1007–1015.
[59] G.G. Li, C.C. Lin, Y. Wei, Z.W. Quan, Y. Tian, Y. Zhao, T.−S. Chan, J. Lin, Chem. Commun. 52 (2016) 7376–7379.
[60] H. Daicho, T. Iwasaki, K. Enomoto, Y. Sasaki, Y. Maeno, Y. Shinomiya, S. Aoyagi, E. Nishibori, M. Sakata, H. Sawa, S. Matsuishi, H. Hosono, Nat. Commun. 3 (2012) 1132.
[61] J. Ding, H. You, Y. Wang, B. Ma, X. Zhou, X. Ding, Y. Cao, H. Chen, W. Geng, Y. Wang, J. Mater. Chem. C 6 (2018) 3435–3444.
[62] S.K. Sharma, Y.−C. Lin, I. Carrasco, T. Tingberg, M. Bettinelli, M. Karlsson, J. Mater. Chem. C 6 (2018) 8923–8933.
[63] K.A. Denault, J. Brgoch, M.W. Gaultois, A. Mikhailovsky, R. Petry, H. Winkler, S. P. DenBaars, R. Seshadri, Chem. Mater. 26 (2014) 2275–2282.
[64] M. Wang, S.H. Zhang, Q.Q. Zhu, Z.W. Zhang, L. Zhang, X. Wang, L.B. Zhang, Y. J. Zhao, X. Xu, L.J. Yin, J. Phys. Chem. C 123 (2019) 3110–3114.
[65] Y.−C. Lin, P. Erhart, M. Bettinelli, N.C. George, S.F. Parker, M. Karlsson, Chem. Mater. 30 (2018) 1865–1877.
[66] J. Zhong, W. Zhao, Y. Zhuo, C. Yan, J. Wen, J. Brgoch, J. Mater. Chem. C 7 (2019) 654–662.